ICIP 2017

AUTOMATIC 3D MODELLING FOR PROSTATE CANCER BRACHYTHERAPY

Mohammad Ali Jan Ghasab[1], *Andrew P. Paplinski*[1], *John M. Betts*[1], *Hayley M. Reynolds*[2], *Annette Haworth*[2,3]

[1]Faculty of Information Technology, Monash University
[2] Sir Peter MacCallum Department of Oncology, The University of Melbourne
[3] School of Physics, The University of Sydney

ABSTRACT

3D visualisation is being used increasingly to improve the accuracy of biopsies and seed placement for prostate cancer brachytherapy (the implantation of small radioactive 'seeds' for radiotherapy). The construction of a 3D model requires the segmentation of 2D Magnetic Resonance (MR) images, which remains a challenging problem. The current practice of manual segmentation requires a very high level of expertise and is time-consuming. In this paper, we propose a new method for creating a 3D model of the prostate from MR images obtained pre-operatively. To do this, an Active Appearance Model (AAM) is created from the image data by grouping the MR images based on the region of the prostate each is taken from. A fast optimisation algorithm is then used to segment a new prostate using the AAM. Our results show that this method is fast and accurate compared with manual segmentation enabling this method to be used intra-operatively.

Index Terms— Medical Image Analysis, Visualisation, Segmentation, Prostate Modelling

1. INTRODUCTION

Prostate cancer is one of the most commonly occurring cancers amongst males in many developed countries. The Australian Institute of Health and Welfare (2015) estimates the annual age-standardised incidence of prostate cancer at 126 cases per 100,000 males [1]. Visualisation of the prostate is being used increasingly to improve the accuracy of medical procedures such as biopsies, and to guide seed placement during brachytherapy - which is a form of radiotherapy achieved by the temporary or permanent implantation of small radioactive 'seeds'.

Ultrasound can be used for intra-operative guidance, however, it does not contain the necessary anatomical detail or resolution for accurate biopsy or seed placement. To provide this anatomical detail our research goal is to co-register the ultrasound with MRI. The method described here provides for rapid and accurate segmentation in 3D space, which is necessary for the intra-operative co-registration with ultrasound.

3D models of the prostate are typically constructed from a set of (two dimensional) image slices made at intervals, and then stacked to create the volumetric form. These images may be created by Magnetic Resonance (MR), as in this research, or ultrasound. An important stage in the creation of the 3D model is the segmentation of the prostate gland in the pre-operative images. However, automatic segmentation is a non-trivial task due to the prostate gland being a soft organ, subject to shape deformations caused by factors such as bladder volume or rectal wall motion. As a consequence manual segmentation is still used extensively, which is too slow for the creation of 3D models intra-operatively, and automatic segmentation of the prostate remains an active research area.

To segment images using region-based level sets, statistical information about the prostate and surrounding region is extracted to maximise the margin between background and prostate regions. A deformable model is implicitly defined and propagated until the two regions converge, at which point the model energy is minimum [2].

Atlas based approaches specify the prostate model by a set of manually labeled images of the organ, which are aligned and registered to reference coordinates [3, 4].

Edge-based methods mainly use gradient filters and multilevel derivatives to detect the prostate boundary [5, 6, 7]. However, these approaches often result in broken and false edges due to the heterogeneous intensity distribution within the prostate gland boundary.

Deformable model methods attempt to represent the shape of an object by reconciling external and internal energies [8]. External energies deform an initial model towards edge points of the object, whereas smoothness of the contour is preserved by internal energy. These energies are combined, and segmentation is achieved by minimising the combined energy function. In recent research, deformable model methods have shown a high potential for application to prostate segmentation since they can address the many possible variations of the prostate shape during the training phase to rebuild and improve the model [9, 10, 11]. Consequently, we are adapting and extending this approach in the current research.

In this work, a 3D Active Appearance Model (AAM) is created from a set of 2D slices. The collection of slices contains information about the prostate surface (the shape component of the AAM) and the volumetric contents of the prostate (the texture component of the AAM). A computa-

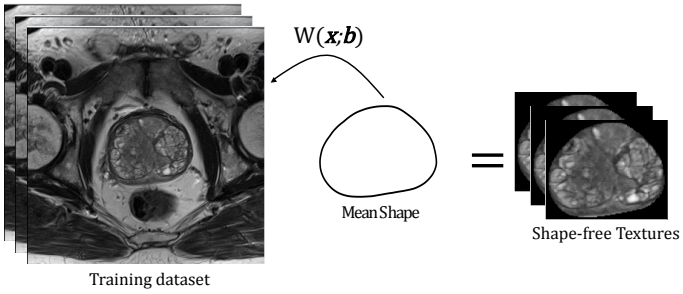

Fig. 1: Prostate appearance warping using a piecewise affine function

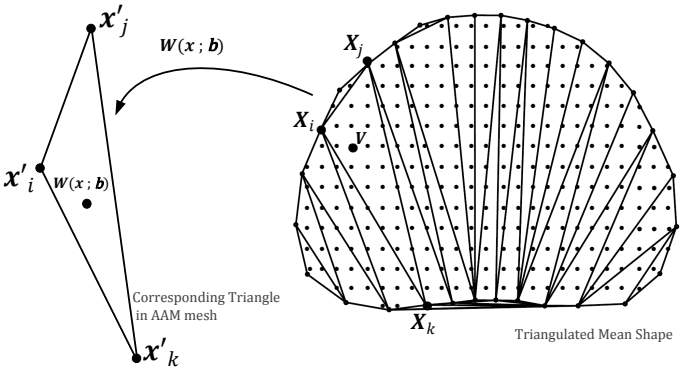

Fig. 2: Prostate shape triangulation with piecewise affine warping

tionally efficient procedure is used to form the 3D model of the prostate by grouping slices in the training data (that is, each MR image) by their corresponding axial position. An improved Inverse Compositional Model Alignment (ICMA) method is used as an optimization algorithm to efficiently segment the prostate.

2. PROSTATE SEGMENTATION METHODOLOGY

To segment the prostate from MR images, a typical model of the gland is created using an AAM [12, 13]. The two phases of this process are: creating the AAM, and fitting to a new unsighted image.

2.1. Creating the Active Appearance Model

An AAM of the prostate is created by modelling both shape and gray-scale (texture) information. These are now discussed in turn.

2.1.1. Shape Model

To create a shape model of the prostate the following steps are performed. Landmarks are annotated in each training image, shape vectors are aligned, and PCA applied to extract significant dimensions [14]. The shape model is

$$\boldsymbol{x} = \bar{\boldsymbol{x}} + \Phi \boldsymbol{b}, \tag{1}$$

where $\bar{\boldsymbol{x}}$ is mean *(reference)* shape of the prostate. The vector of shape parameters $\boldsymbol{b}$ specifies possible variations of the prostate along with its principal components ϕ.

2.1.2. Texture Model

A texture model of the prostate is constructed by sampling voxels from the prostate in each training image and mapping them to the mean shape using a piecewise affine warping $W(\boldsymbol{x}; \boldsymbol{b})$. This results a set of shape-free textures patches as shown in Figure 1. Delaunay triangulation is used to warp an image $I_{(x,y)}$ and sample voxels (using bilinear interpolation) in the image coordinates $I(W(\boldsymbol{x}; \boldsymbol{b}))$, and map the sampled intensity values to the corresponding locations (pixels) in the mean shape coordinates. Each pixel $\boldsymbol{v}$ in the mean shape is located inside a triangle, for example, $(\boldsymbol{x}_i, \boldsymbol{x}_j, \boldsymbol{x}_k)$, as shown in Figure 2.

Once computed, the warp function is applied to each training image and voxel samples to create a gray-scale vector $\boldsymbol{g_{im}}$ containing intensity values of the prostrate. This is usually normalised to remove effects of illumination and lighting variation. The resulting texture model is

$$\boldsymbol{g} = \bar{\boldsymbol{g}} + \Omega \boldsymbol{c}, \tag{2}$$

where $\bar{\boldsymbol{g}}$ is the average of all gray-scale vectors, Ω is the significant modes of texture variation and $\boldsymbol{c}$ denotes the texture parameters. As with the shape model, Ω is calculated by applying PCA to a matrix of gray-scale vectors to reduce dimensionality. Having created the texture model, the appearance of any prostate image in training dataset can be reconstructed by Equation (2) and corresponding texture parameters.

2.1.3. Creating a 3D model of the Prostate

The previous subsections (2.1.1 and 2.1.2) showed how a 2D AAM could be created for single slice of the 3D prostate volume. To create the 3D AAM (of the whole prostate) these steps can be performed for each level in the image stack corresponding to sections at different depths in the prostate. To train the AAM in this way, training data sets are created at each depth. Each AAM can then be trained independently in parallel. A a surface model of the prostate can then be formed from the stack of 2D AAMs, each explaining a particular part of the prostate. A prostate surface along with its possible shape variations created in this way is shown in Figure 3.

2.2. Fitting the Active Appearance Model

Fitting a 3D AAM of the the prostate to a new, unsighted, image requires non-linear optimisation [15]. The difference be-

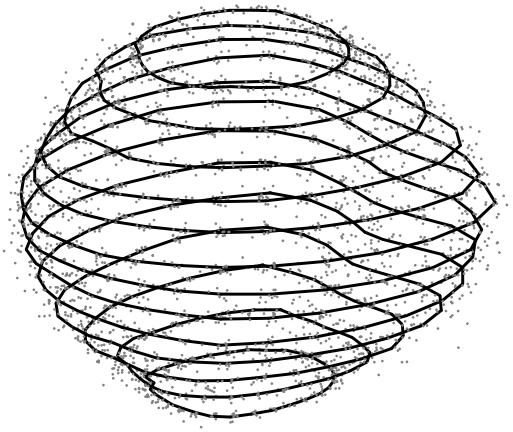

Fig. 3: A 3D model of the prostate showing shape variations

tween a synthesised prostate image (obtained from the AAM) and the test image is measured using non-linear least squares, giving the objective function

$$E(\boldsymbol{q}) = \arg\min \Big[T(\boldsymbol{x}) - I(W(\boldsymbol{x};\boldsymbol{b}))\Big]^2 \qquad \boldsymbol{q} = \begin{bmatrix}\boldsymbol{b} & \boldsymbol{c}\end{bmatrix}^T, \tag{3}$$

where $T(\boldsymbol{x})$ is a synthesised prostate image (obtained from $\bar{\boldsymbol{g}}$) and $I(W(\boldsymbol{x};\boldsymbol{b}))$ is the warped test image with respect to shape parameters $\boldsymbol{b}$. The fitting goal is then to minimise $E(\boldsymbol{q})$ with respect to shape parameters $\boldsymbol{b}$ and the texture parameters $\boldsymbol{c}$. Although gradient descent is a well-known optimisation method for this type of NLS problem, it is computationally slow and inefficient because the image gradient, Jacobian, and Hessian matrices need to be calculated at each iteration. To overcome this issue, the fitting problem is redefined as an image alignment problem, where a modified version of Lucas-Kanade method known as Inverse Compositional Model Alignment (ICMA) gives a more efficient fitting process [16, 17].

The ICMA algorithm performs Gauss-Newton gradient descent simultaneously on the warp function $W(\boldsymbol{x};\boldsymbol{b})$ with respect to shape parameters $\boldsymbol{b}$ and texture parameters $\boldsymbol{c}$. The main difference between the ICMA algorithm and conventional gradient descent is that, instead of updating the shape parameters incrementally ($\boldsymbol{b} \longleftarrow \boldsymbol{b}+\delta\boldsymbol{b}$), it updates the warping function in an inverse compositional manner. This leads to pre-computing the Jacobian and image gradient matrices, reducing the computation required. Updating at each iteration (t) is

$$W_{t+1}(\boldsymbol{x};\boldsymbol{b}) \leftarrow W_t(W(\boldsymbol{x};\delta\boldsymbol{b})^{-1};\boldsymbol{b}) \leftarrow W_t(\boldsymbol{x};\boldsymbol{b}) \circ W(\boldsymbol{x};\delta\boldsymbol{b})^{-1}, \tag{4}$$

where $\circ$ denotes the compositional operation. $W(\boldsymbol{x};\delta\boldsymbol{b})^{-1}$ is the inverted incremental warp, which is computed with respect to the synthesised image $T(\boldsymbol{x})$ rather than the test image $I(W(\boldsymbol{x};\boldsymbol{b}))$. Reversing the role of the synthesised image and the test image in Equation (3), and taking a first order Taylor expansion establishes the ICMA algorithm. The objective function is now

$$E(\delta\boldsymbol{q}) = \arg\min_{\delta\boldsymbol{b},\delta\boldsymbol{c}} \Big|\Big|T(\boldsymbol{x}) + \Omega\boldsymbol{c} - I(W(\boldsymbol{x};\boldsymbol{b})) + J\delta\boldsymbol{b} + \Omega\delta\boldsymbol{c}\Big|\Big|^2 \qquad \delta\boldsymbol{q} = \begin{bmatrix}\delta\boldsymbol{b} & \delta\boldsymbol{c}\end{bmatrix}^T. \tag{5}$$

The error between the given image and the model instance in Equation (5) is simultaneously minimised using an ℓ_2 norm with respect to model parameters. This requires the steepest descent image ($J\delta\boldsymbol{b} + \Omega\delta\boldsymbol{c}$) to be calculated at every iteration because it depends on the texture parameters $\delta\boldsymbol{c}$. A faster optimization method is introduced using the iterative scheme described in [18], where Equation (5) is minimised with respect to each parameter $\delta\boldsymbol{c}$ and $\delta\boldsymbol{b}$ in turn, that is,

$$\arg\min_{\delta\boldsymbol{b},\delta\boldsymbol{c}} E(\delta\boldsymbol{b},\delta\boldsymbol{c}) = \min_{\delta\boldsymbol{b}} \Big[\min_{\delta\boldsymbol{c}} E(\delta\boldsymbol{b},\delta\boldsymbol{c})\Big]. \tag{6}$$

Thus Equation (5) is first optimised with respect to $\delta\boldsymbol{c}$ as

$$\delta\boldsymbol{c} = \Omega^T\Big(I(W(\boldsymbol{x};\boldsymbol{b})) - T(\boldsymbol{x}) - \Omega\boldsymbol{c} - \nabla T\frac{\partial W}{\partial \boldsymbol{b}}\delta\boldsymbol{b}\Big). \tag{7}$$

The solution to Equation (7) (a function of $\delta\boldsymbol{b}$) is fed back into Equation (5), which is then optimised with respect to $\delta\boldsymbol{b}$ giving

$$\delta\boldsymbol{b} = H^{-1}\Psi^T\Big(I(W(\boldsymbol{x};\boldsymbol{b})) - T(\boldsymbol{x})\Big), \tag{8}$$

where H and Ψ are Hessian and steepest descent matrices, respectively, calculated as follows:

$$\Psi = \Big(\nabla T\frac{\partial W}{\partial \boldsymbol{b}}\Big) - \Omega\Omega^T\Big(\nabla T\frac{\partial W}{\partial \boldsymbol{b}}\Big) \quad ; \quad H = \Psi^T\Psi. \tag{9}$$

These steps are repeated at each iteration and model parameters are updated accordingly until the stopping criteria is met. The texture parameters are updated in a common additive manner ($\boldsymbol{c} \leftarrow \boldsymbol{c} + \delta\boldsymbol{c}$), while the shape parameters are indirectly updated using Equation (4).

Table 1: Accuracy of segmentation using leave-one-out cross validation on 10 cases during the model training phase

Metrics	Mean	Median
DSC	0.82	0.83
95% HD	19.48	20.91

Table 2: Accuracy of the proposed method tested on unsighted images adjacent to mid-gland

Name	95% HD	DSC
Case 26	12.94	0.91
Case 27	20.51	0.80
Case 28	9.8	0.94
Case 29	15.5	0.92
Case 30	19.31	0.84
Case 31	23	0.82
Case 32	11.77	0.90
Case 33	13.07	0.85
Case 34	21.56	0.80
Case 36	28.17	0.90
Average	**17.56**	**0.87**

3. SETUP AND RESULTS

A subset of the MICCAI[1] data set was used to construct an AAM of the prostate gland. The model was created from 10 cases, having an average voxel size of $0.3905 \times 0.3905 \times 3.3$ mm. Leave-One-Out Cross Validation (LOOCV) was used to evaluate the performance of the proposed algorithm during training. This meant that each image was removed in turn from the training set and a model created. The image that had been removed was then automatically segmented using the model. Two common measures of: Dice Similarity Coefficient (DSC) and 95th% Hausdorff Distance (95% HD) were used to measure accuracy of the segmentation results against a manually segmented reference. Segmentation using LOOCV results in a mean DSC of 0.82 and a median DSC of 0.83 during the training phase, as shown in Table 1.

Accuracy of the model was then evaluated by automatically segmenting 10 cases adjacent to the mid-gland, which had not been included in the data set for model building. The results in Table 2 shows an average accuracy of 87% for the segmentation of unsighted images using the proposed algorithm. Figure 4 shows the qualitative results of prostate segmentation using the ICMA algorithm for each of the 10 cases in the test data set. It can be seen that a wide variety of MR images was used to evaluate the proposed method under a variety of difficult conditions, including poor contrast and deformations of the prostate.

[1] http://promise12.grand-challenge.org/

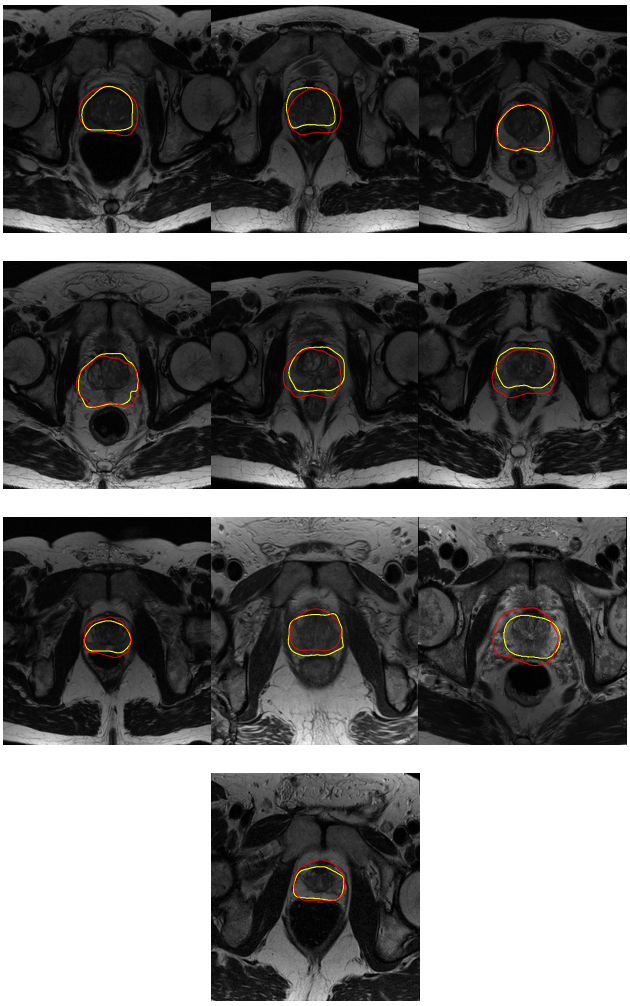

Fig. 4: Qualitative segmentation results of 10 cases (from upper left) using ICMA algorithm.The segmented prostates with ICMA method and reference are shown with red and yellow respectively.

4. CONCLUSION

We have presented a new method for creating a 3D model of the prostate from MR images obtained pre-operatively. This was achieved by fitting an Active Appearance Model to image data that had been grouped by the location in the prostate it was taken from. This meant that the training data was comprised of subsets that were more homogeneous, better describing the region each represented compared with other methods. A fast, inverse compositional alignment algorithm was then applied to segment a new prostate. Our method was tested on a small subset of the MICCAI database, segmenting mid-gland slices. Results show that the automatically segmented images are accurate, compared with manual segmentation.

5. REFERENCES

[1] AIHW, "Cancer incidence projections: Australia 2011 to 2020," .

[2] Soumya Ghose, Arnau Oliver, Robert Martí, Xavier Lladó, Joan C Vilanova, Jordi Freixenet, Jhimli Mitra, Désiré Sidibé, and Fabrice Meriaudeau, "A survey of prostate segmentation methodologies in ultrasound, magnetic resonance and computed tomography images," *Computer methods and programs in biomedicine*, vol. 108, no. 1, pp. 262–287, 2012.

[3] Mathieu De Craene, Aloys du Bois dAische, Benoît Macq, and Simon K Warfield, "Multi-subject registration for unbiased statistical atlas construction," in *International Conference on Medical Image Computing and Computer-Assisted Intervention*. Springer, 2004, pp. 655–662.

[4] Carole J Twining, Tim Cootes, Stephen Marsland, Vladimir Petrovic, Roy Schestowitz, and Chris J Taylor, "A unified information-theoretic approach to groupwise non-rigid registration and model building," in *Biennial International Conference on Information Processing in Medical Imaging*. Springer, 2005, pp. 1–14.

[5] Reyer Zwiggelaar, Yanong Zhu, and Stuart Williams, "Semi-automatic segmentation of the prostate," in *Iberian Conference on Pattern Recognition and Image Analysis*. Springer, 2003, pp. 1108–1116.

[6] Maryam Samiee, Gabriel Thomas, and Reza Fazel-Rezai, "Semi-automatic prostate segmentation of MR images based on flow orientation," in *Signal processing and information technology, 2006 IEEE International Symposium on*. IEEE, 2006, pp. 203–207.

[7] Daniel Flores-Tapia, Gabriel Thomas, Niranjan Venugopal, Boyd McCurdy, and Stephen Pistorius, "Semi automatic MRI prostate segmentation based on wavelet multiscale products," in *2008 30th Annual International Conference of the IEEE Engineering in Medicine and Biology Society*. IEEE, 2008, pp. 3020–3023.

[8] Tim McInerney and Demetri Terzopoulos, "Deformable models in medical image analysis: a survey," *Medical image analysis*, vol. 1, no. 2, pp. 91–108, 1996.

[9] Yanong Zhu, Stuart Williams, and Reyer Zwiggelaar, "A hybrid ASM approach for sparse volumetric data segmentation," *Pattern recognition and image analysis*, vol. 17, no. 2, pp. 252–258, 2007.

[10] Nasr Makni, Philippe Puech, Renaud Lopes, Anne-Sophie Dewalle, Olivier Colot, and Nacim Betrouni, "Combining a deformable model and a probabilistic framework for an automatic 3D segmentation of prostate on MRI," *International journal of computer assisted radiology and surgery*, vol. 4, no. 2, pp. 181–188, 2009.

[11] Robert Toth, Pallavi Tiwari, Mark Rosen, Galen Reed, John Kurhanewicz, Arjun Kalyanpur, Sona Pungavkar, and Anant Madabhushi, "A magnetic resonance spectroscopy driven initialization scheme for active shape model based prostate segmentation," *Medical Image Analysis*, vol. 15, no. 2, pp. 214–225, 2011.

[12] Timothy F Cootes, Gareth J Edwards, and Christopher J Taylor, "Active appearance models," in *European conference on computer vision*. Springer, 1998, pp. 484–498.

[13] Timothy F Cootes, Gareth J Edwards, Christopher J Taylor, et al., "Active appearance models," *IEEE Transactions on pattern analysis and machine intelligence*, vol. 23, no. 6, pp. 681–685, 2001.

[14] Timothy F Cootes, Christopher J Taylor, David H Cooper, and Jim Graham, "Active shape models-their training and application," *Computer vision and image understanding*, vol. 61, no. 1, pp. 38–59, 1995.

[15] Simon Baker and Iain Matthews, "Lucas-Kanade 20 years on: A unifying framework," *International journal of computer vision*, vol. 56, no. 3, pp. 221–255, 2004.

[16] Iain Matthews and Simon Baker, "Active appearance models revisited," *International Journal of Computer Vision*, vol. 60, no. 2, pp. 135–164, 2004.

[17] Ralph Gross, Iain Matthews, and Simon Baker, "Generic vs. person specific active appearance models," *Image and Vision Computing*, vol. 23, no. 12, pp. 1080–1093, 2005.

[18] Georgios Tzimiropoulos and Maja Pantic, "Optimization problems for fast AAM fitting in-the-wild," in *Proceedings of the IEEE international conference on computer vision*, 2013, pp. 593–600.